The Astrophysical Journal, 704:1433–1447, 2009 October 20 doi:10.1088/0004-637X/704/2/1433

A 31 GHz SURVEY OF LOW-FREQUENCY SELECTED RADIO SOURCES

B. S. Mason[1], L. Weintraub[2], J. Sievers[3], J. R. Bond[3], S. T. Myers[4], T. J. Pearson[2], A. C. S. Readhead[2], and M. C. Shepherd[2]

[1] National Radio Astronomy Observatory, 520 Edgemont Road, Charlottesville, VA 22903, USA
[2] Owens Valley Radio Observatory, California Institute of Technology, Pasadena, CA, USA
[3] Canadian Institute for Theoretical Astrophysics, University of Toronto, ON M5S 3H8, Canada
[4] National Radio Astronomy Observatory, Soccorro, NM 87801, USA
Received 2009 February 2; accepted 2009 August 26; published 2009 October 2

ABSTRACT

The 100 m Robert C. Byrd Green Bank Telescope and the 40 m Owens Valley Radio Observatory telescope have been used to conduct a 31 GHz survey of 3165 known extragalactic radio sources over 143 deg^2 of the sky. Target sources were selected from the NRAO VLA Sky Survey in fields observed by the Cosmic Background Imager (CBI); most are extragalactic active galactic nuclei (AGNs) with 1.4 GHz flux densities of 3–10 mJy. The resulting 31 GHz catalogs are presented in full online. Using a maximum-likelihood analysis to obtain an unbiased estimate of the distribution of the 1.4–31 GHz spectral indices of these sources, we find a mean 31–1.4 GHz flux ratio of 0.110 ± 0.003 corresponding to a spectral index of $\alpha = -0.71 \pm 0.01$ ($S_\nu \propto \nu^\alpha$); $9.0\% \pm 0.8\%$ of sources have $\alpha > -0.5$ and $1.2\% \pm 0.2\%$ have $\alpha > 0$. By combining this spectral-index distribution with 1.4 GHz source counts, we predict 31 GHz source counts in the range 1 mJy $< S_{31} <$ 4 mJy, $N(> S_{31}) = (16.7 \pm 1.7)$ deg^{-2} $(S_{31}/1\ \mathrm{mJy})^{-0.80\pm0.07}$. We also assess the contribution of mJy-level ($S_{1.4\,\mathrm{GHz}} < 3.4$ mJy) radio sources to the 31 GHz cosmic microwave background power spectrum, finding a mean power of $\ell(\ell+1)C_\ell^{\mathrm{src}}/(2\pi) = 44 \pm 14\ \mu\mathrm{K}^2$ and a 95% upper limit of 80 μK^2 at $\ell = 2500$. Including an estimated contribution of 12 μK^2 from the population of sources responsible for the turn-up in counts below $S_{1.4\,\mathrm{GHz}} = 1$ mJy, this amounts to $21\% \pm 7\%$ of what is needed to explain the CBI high-ℓ excess signal, $275 \pm 63\ \mu\mathrm{K}^2$. These results are consistent with other measurements of the 31 GHz point-source foreground.

Key words: cosmic microwave background – cosmology: observations – galaxies: active – radio continuum: galaxies

Online-only material: color figures, machine-readable tables

1. INTRODUCTION

Accurate measurements of cosmic microwave background (CMB) anisotropies on scales smaller than the sound horizon at last scattering are necessary to form a complete understanding of the initial power spectrum of cosmic inhomogeneities. Secondary anisotropies—chiefly reionization and Sunyaev–Zel'dovich (SZ) distortions from large-scale structures—also leave imprints on these scales which contain clues of the subsequent evolution of structures from very simple, linear initial conditions to the wealth of nonlinear structures seen in the nearby universe. Photon diffusive damping occurring near last scattering has the effect of strongly suppressing small-scale intrinsic CMB anisotropies, so precise measurements on these scales are difficult. A key challenge for centimeter-wavelength observations on these angular scales is the foreground presented by faint, discrete radio sources.

The Cosmic Background Imager (CBI; Readhead et al. 2004) is a 30 GHz, small angular-scale experiment which has detected, at 2.9σ, power in excess of intrinsic CMB anisotropy at multipoles $\ell > 2000$. The accuracy of this result is limited by our knowledge of the contribution of faint extragalactic radio sources to the measured power spectrum. The CBI removes all *known* radio sources by "projecting" them out of the data set.[5] The best available low-frequency radio data covering the CBI fields are from the 1.4 GHz NRAO VLA Sky Survey (NVSS; Condon et al. 1998), which is reliable and complete down to 3.4 mJy. Since the source density on the sky as a function of flux density (the "source counts") is well known to down to 50–100 μJy, the 31 GHz power spectrum of sources not detected in the NVSS can be calculated given sufficient knowledge of the ratio of flux densities at these two frequencies, $S_{30}/S_{1.4}$. Since the sources are unresolved they will have a flat power spectrum: $C_\ell \sim$ const, or $\ell(\ell+1)C_\ell \sim \ell^2$ in terms of the prevailing convention for CMB power spectra. The power spectrum of these sources is directly subtracted from the CBI power spectrum. In this paper, we call this correction to the power spectrum the "residual source correction"; in other papers it is also called the statistical correction and the isotropic point-source correction. The uncertainty in this correction is comparable to other uncertainties on the smallest angular scales measured by CBI ($\ell > 2000$, or angular scales smaller than about 5 arcminutes). Readhead et al. (2004) calculate a value of $96 \pm 48\ \mu\mathrm{K}^2$, where the uncertainty in the correction is dominated by the poorly constrained extrapolation of 1.4 GHz flux densities to 31 GHz. The $\sim 50\ \mu\mathrm{K}^2$ uncertainty in the point-source correction contributes a substantial uncertainty to the CBI measurement at $\ell > 1960$ of $355^{+137}_{-122}\ \mu\mathrm{K}^2$ (of which 80–90 μK^2 is expected to be intrinsic anisotropy). New CBI results presented in Sievers et al. (2009) show an excess which, to be explained by point sources, would have a power $\ell(\ell+1)C_\ell^{\mathrm{src}}/(2\pi) = 275 \pm 63\ \mu\mathrm{K}^2$ at $\ell = 2500$, consistent with the Readhead et al. (2004) result.

In more detail, if at a given frequency sources above some flux density S_{max} are dealt with, the power spectrum of residual

[5] "Source projection" is a procedure equivalent to allowing an arbitrary variance from a linear combination of the data corresponding to the point source. This procedure is performed in fourier space; the analog in the image domain would be deleting a contaminated pixel.

sources below $S_{\rm max}$ is proportional to (Myers et al. 2003)

$$X_{\rm src} = \int_0^{S_{\rm max}} dS\, S^2 \frac{dN}{dS}. \quad (1)$$

In our case, the sources are selected for inclusion at a different lower frequency (i.e., they are in effect the sources in our fields that are not detected reliably in the NVSS, hence are not projected out). Then, assuming that the spectral properties of the sources are constant over the range of relevant flux densities—in practice, $\sim$ 1–4 mJy at 1.4 GHz—Equation (1) becomes

$$X_{\rm src} = \left\langle \left(\frac{S_{31}}{S_{1.4}}\right)^2 \right\rangle \int_0^{S_{\rm max,1.4}} dS_{1.4}\, S_{1.4}^2 \frac{dN}{dS_{1.4}}. \quad (2)$$

The low-frequency source counts dN/dS are well known. To accurately correct 31 GHz CMB measurements for point-source contamination, we need to determine the mean value of $(S_{31}/S_{1.4})^2$, and to determine the uncertainty in $X_{\rm src}$ and therefore in the source-corrected CMB power spectrum, we must know its distribution. For the shallow source counts [$N(>S) \propto S^{-0.7}$] observed at mJy levels, the sources immediately below the projection threshold dominate the sky variance and our surveys target this population. For the CBI, for instance, 75% of the correction comes from sources in the range $1 < S_{1.4} < 3.4$ mJy. At 31 GHz, the sky variance can be strongly influenced by the abundance of comparatively rare flat or inverted-spectrum sources, so a large sample is needed to place useful constraints on the abundance of these sources.

In this paper, we present a detailed characterization of the impact of the discrete source foreground on arcminute-scale 31 GHz anisotropy measurements based upon two observational campaigns. The first campaign was carried out with the Owens Valley Radio Observatory (OVRO) 40 m telescope at 31 GHz from 2000 September through 2002 December. The second campaign used the Robert C. Byrd Green Bank Telescope (GBT) from 2006 February to May. This work was undertaken with the specific aim of improving the accuracy of CBI microwave background anisotropy measurements. A companion paper (Sievers et al. 2009) presents the five-year CBI total intensity power spectrum incorporating the results of the point-source measurements discussed here.

The structure of this paper is as follows. In Section 2, we describe the instrumentation used in both surveys. Section 3 describes the source lists and sample selection, and Section 4 describes the OVRO 40 m and GBT observations and data reduction and presents catalogs of the observations. Section 5 presents a determination of the 1.4–31 GHz spectral index of NVSS sources and determines the implications of these measurements for 31 GHz CMB observations, for the case of the CBI in particular; here, we also present a determination of the 31 GHz source counts. Finally, Section 6 reviews our main conclusions.

2. INSTRUMENTATION

2.1. OVRO 40 m and 31 GHz Receiver

In 1999, the OVRO 40 m telescope was outfitted with a Dicke-switching, dual horn receiver operating in four 2 GHz bands between 26 and 34 GHz. The Dicke switch alternates between the two horns at a rate of 125 Hz, sampling two beams separated by 7.′8 in cross-elevation on the sky. Each beam has a FWHM of 1.′36 at 31 GHz; this is somewhat larger than what would be expected for a 40 m dish since only the central 30 m are illuminated. The measured receiver temperature in the 31 GHz band is 23 K. The statistics of (noise) samples taken against both ambient temperature and 77 K beam-filling loads are consistent with the receiver temperature. Including 13 K per air mass due to the atmosphere, 2.7 K from the CMB, and a fixed ground contribution of 10 K, the system temperature at zenith is $\sim$ 50 K. Calibration is facilitated by two broadband noise diodes; cross-guide couplers before the Dicke switch allow for the insertion of signals from these devices.

The telescope is an alt-azimuth instrument consisting of a paraboloidal dish reflector, primary focus feed, and supports, mounted on an alidade and base pedestal. Our observing frequency of 31 GHz is beyond the design specification of the 40 m telescope, resulting in aperture efficiencies of only 15%. The gain of the 40 m changes as a function of both zenith angle (ZA) due to gravitational deformations in the dish structure, and of angle of the Sun from the optical axis due to thermal deformations. These variations were characterized by long tracks on bright calibrators and the resulting gain corrections are applied offline in the data reduction. The focus position also varies with ZA. The focus position corrections are applied in real time and checked periodically for consistency. The peak sensitivity that the 40 m achieves is 12 mJy root mean square (rms) in 1 minute at 40° elevation in the 31 GHz band. The outer bands had substantially higher noise levels. The analysis in this paper relies upon data from the 31 GHz channel only.

2.2. GBT, 31 GHz Receiver and Continuum Back End

The GBT is a 100 m off-axis Gregorian telescope located in Green Bank, West Virginia (Jewell & Prestage 2004). One of the GBT's distinguishing features is the fact that it was designed to operate efficiently at frequencies up through 115 GHz. For the observations presented here, the GBT's 31 GHz aperture efficiency was 50%. The two-dimensional rms referenced pointing accuracy is 4″ on timescales of half an hour to an hour. Corrections to the focus tracking model on the same timescale are typically a few millimeters. Owing to the primary reflector's remotely actuated positioning system, the telescope gain does not vary significantly at elevations greater than 20°.

Broadband measurements of the radio-frequency (RF) continuum are affected by systematic effects such as gain fluctuations and variation in the emissivity of the atmosphere. To this end, the receiver built for the OVRO 40 m employed a Dicke switch, enabling two feeds to be sampled rapidly in series. For the GBT receiver, we chose an electronic beam-switching arrangement employing 180° hybrids similar to the *WMAP* radiometers (Jarosik et al. 2003; Padin 2001). This permits wider bandwidth coverage, avoids expensive and difficult to procure Dicke switches, and permits signals from both feeds to be simultaneously measured at all times. The receiver provides 16 continuum channels, one for each of four frequency bands, two feeds, and both circular polarizations. Receiver temperatures range from 20 K to 40 K across the band, resulting in $T_{\rm sys}$ values on-sky of 35–65 K. Broadband noise diodes are coupled in to the signal path prior to the first hybrid tee and permit monitoring the total gain of the system for calibration purposes.

The Caltech Continuum Backend (CCB) is a digital back end which controls the GBT 26–40 GHz receiver and synchronously reads out and demodulates the beam-switched signal. Lab tests conducted with the CCB connected to the receiver show that the noise obtained is 15%–30% above the theoretical noise

minimum given by the radiometer equation. For our observations, we operated the receiver with a 4 kHz beam-switch rate in order to avoid excessive lost of time to blanking after phase switch transitions. The CCB was constructed by NRAO and the California Institute of Technology, with funding provided to Caltech through the NRAO University Instrumentation Program. The 26–40 GHz receiver and CCB are available as facility instruments on the GBT.

With the 31 GHz receiver and continuum back end, we attain nearly thermal noise limited performance (∼0.15 mJy rms in 1 minute) a small fraction of the time, when the atmosphere is very dry and stable. More typically, the thermal noise rms in a 60 s double-differenced observation (essentially identical to that described in Section 4.1) is 0.2–0.4 mJy (rms). The results in this paper depend only on data from the 31 GHz channels.

3. SOURCE LISTS AND SAMPLE SELECTION

The CBI total intensity mosaic fields (Readhead et al. 2004) covered 98 deg^2 of sky, including a 45′ buffer zone. The OVRO 40 m survey targeted all $S_{1.4} > 6$ mJy sources in this region. The CBI polarization observations (Sievers et al. 2007) covered 115 deg^2 in all, also including a 45′ buffer zone; accounting for the overlap between these two data sets the total sky coverage is 143 deg^2. The GBT survey targeted $S_{1.4} > 3.4$ mJy (the NVSS 99% completeness limit) sources in this total region, although full coverage was not achieved. Source selection proceeded from areas of sky with the lowest CBI map noise. Sources detected at 3σ or greater in the OVRO survey as a rule were avoided in the GBT survey.

Sources in the CBI fields were observed from 1999 September through 2001 December with the OVRO 40 m telescope in support of ongoing CBI observations. The 40 m observations preferentially targeted sources in the original (Pearson et al. 2003; Readhead et al. 2004) CBI total intensity fields; in all, 2315 sources were observed by the 40 m. With the typical rms sensitivity of the OVRO survey (2.5 mJy—see Section 4.1), this resulted in 180 detections at 4σ or greater significance (363 at 3σ or greater).

Our aim with the GBT survey was to measure *all* of the NVSS sources in the CBI fields with a sensitivity comparable to the rms noise in the CBI maps. The 363 sources previously detected[6] at 3σ or greater in the OVRO 40 m survey were not observed by the GBT, leaving 5636 sources. Useful GBT data were collected on 1490 of these (Section 4.3). Faint NVSS sources, and sources in areas where the CBI maps are most sensitive, were preferentially targeted. Of the OVRO observations, 640 sources' data were superceded by more sensitive GBT measurements, leaving 1675 unique observations in the OVRO data set. In all useful data were obtained on 3165 NVSS sources. The distribution of 1.4 GHz flux densities of the sources measured is shown in Figure 1.

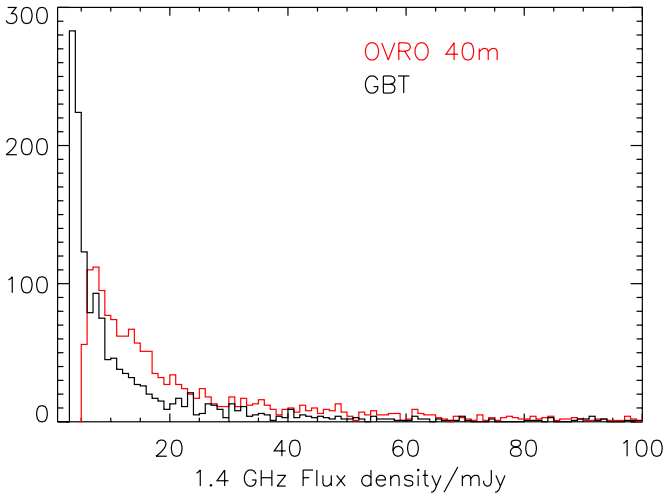

Figure 1. NVSS flux densities for sources measured in the GBT and OVRO 40 m surveys.

(A color version of this figure is available in the online journal.)

4. OBSERVATIONS

4.1. OVRO Observations

All NVSS sources brighter than 6 mJy were observed to a typical rms sensitivity of 2.4 mJy, requiring 30 5 minute observations on average. Five minute observations of NVSS-selected sources were interleaved with daily measurements of 3C286, 3C147, 3C279, and other bright sources to monitor the system's performance. In between calibrator observations, the system gain was monitored with the noise diodes internal to the receiver. Every 40 minutes, a calibrator source within ∼15° of the field being observed was measured to determine the telescope pointing offset. For each flux density measurement, the online system reports an estimate of the measurement error from the variance in the 1 s samples within the integration period. During the course of all observations, weather data are collected and recorded for later correlation with the astronomical datastream. The basic measurement consists of four beam-switched integration periods wherein the source of interest is alternately placed in the two beams of the telescope in an A/B/B/A pattern. This symmetric double-differencing scheme is effective at canceling constant and gradient terms in atmospheric emission (Readhead et al. 1989).

Our flux density scale is based on the *WMAP* five-year measurement of the 32 GHz brightness temperature of Jupiter $T_J = 146.6 \pm 0.75$ K (Hill et al. 2009), extrapolated across the receiver bandpass with 3C286 using an assumed spectral index of $\alpha = -0.827$ (Leitch et al. 2000). Observations of 3C286, 3C48, and 3C147 from 1999 September through 2000 May showed uncorrelated rms variations in flux density of ∼4%. Together with the 3% uncertainty in the absolute flux density of Jupiter, this gives a 5% calibration uncertainty for the OVRO 40 m.

4.2. OVRO Data Reduction

OVRO data were reduced as follows. Observations of the noise diodes several times per hour are first used to remove electronic gain fluctuations and scale the data to antenna temperature. Corrections for the telescope gain as a function of elevation, determined from long tracks on bright calibrators, are applied, as is a correction to account for atmospheric opacity as a function of elevation.

Time-variable weather conditions determine the sensitivity of OVRO 40 m flux density measurements. Typically sources were observed in rotation, with five 1 minute observations of each source. The timescale on which changes in the weather affect the 40 m photometric sensitivity is typically an hour, which sets the timescale on which we wish to estimate the

[6] Due to a software bug, GBT observations of sources between +01° and −01° were observed without regard for the OVRO 40 m measurements, i.e., observations in this range were not precensored by the measured OVRO flux value.

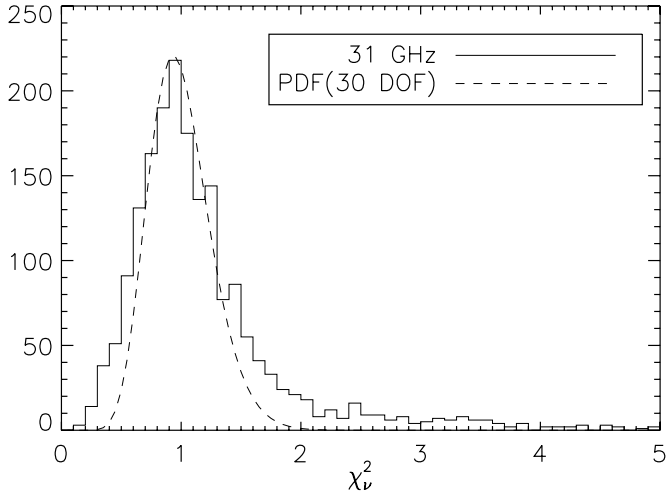

Figure 2. χ^2_ν distribution for OVRO 40 m measurements, each individual χ^2_ν value being derived from the combination of all data in the given frequency band on a given source. Also shown is the theoretical reduced χ^2 distribution for 30 degrees of freedom, which is typical, although the number of observations on a given source ranges from three to a hundred in some cases.

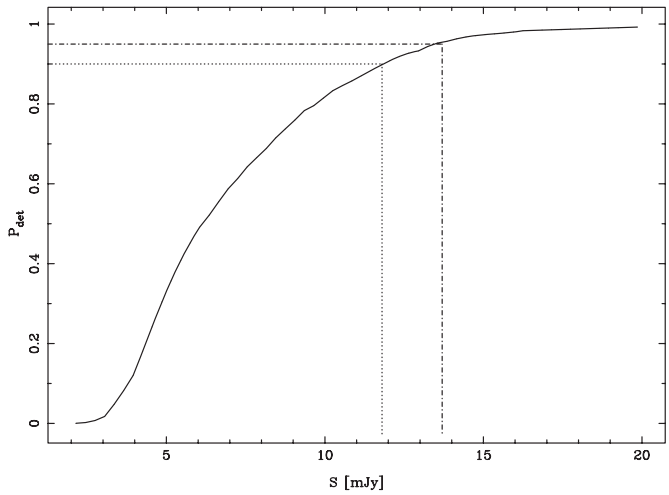

Figure 3. Probability that a given source is detected in the OVRO survey as a function of 31 GHz flux density. The 90% (dotted) and 95% (dash-dotted) completeness levels are shown for clarity. The GBT survey is essentially complete above 2.5 mJy.

measurement noise. During this period of time, ∼10 separate sources with different mean flux densities were measured. Sources in the OVRO sample are expected to have 31 GHz flux densities of 1–2 mJy, small in comparison to the 10–15 mJy noise level achieved on a per-observation basis. To determine the measurement noise for a single observation, we wished to compute the characteristic scatter of similar observations nearby in time with no contribution due to the scatter in the source flux densities themselves, our main concern being the power-law tail of the source flux density distribution which results in rare objects comparable to or greater than the per-observation noise level which could bias a scatter-based noise estimate. We chose to determine the noise level of each observation by computing the median absolute deviation (MedAD) of similar observations within a 1 hr buffer centered on the observation under consideration. The MedAD of some data x_i is defined as

$$\mathrm{MedAD}(x_i) = \mathrm{Median}(|x_i - \mathrm{Median}(x_i)|) \quad (3)$$

and is a measure of the dominant noise scale of a distribution which is extremely resistant to the presence and magnitude of outliers (Hoaglin et al. 1983). For a Gaussian distribution of width σ_g, the MedAD $= 0.6745\sigma_g$. We used this relation to rescale the MedAD into an effective Gaussian σ value for each observation. An independent noise estimate was provided by the scatter of 1 s integrations *within* each measurement. The internal noises gave results comparable to, but generally 15%–30% lower than, the scatter between observations. This is consistent with the expectation that except in the very best observing conditions, low-level photometric instabilities (e.g., a slow variation in the gradient of the sky emission) on timescales longer than that of an individual source observation contribute to the measurement noise. We confirmed with simulations that to within a few percent this approach yields an unbiased estimate of the rms of a Gaussian noise distribution in the presence of power-law source populations with typical per-measurement signal-to-noise ratios of 0.1–0.2.

Over the course of the observing campaign, individual sources in our sample were observed between a few and about 100 times, most commonly about 30 times. All observations of a given source were combined to form a weighted mean and an uncertainty on this mean was computed by propagation of the error bars of each measurement. The reduced χ^2 of the data about this average was also computed; these values are shown in Figure 2. For reference, the expected distribution of χ^2_ν for 30 degrees of freedom (dof) is shown. There is a fairly broad distribution of final sensitivities, owing largely to the range of total integration times per source, but also to the range of photometric conditions. For our final source catalog (Section 4.7), we adopted a 4σ detection threshold; the probability of detecting a random source of a given flux density, allowing for the distribution of noises in our data set, is shown in Figure 3.

We reject data within 5° of the Sun or the Moon, as well as data for which the preceding pointing calibrator observations were not successful or did not occur within 1 hr. Since high winds can affect the telescope pointing, observations during which the wind was greater than 15 mph are discarded. Reducing the pointing requirement from an hour to a half-hour, and the wind limit from 15 to 7.5 mph (reducing the force of the wind on the telescope by roughly a factor of 4) did not significantly affect the measured flux densities of the OVRO-detected sources.

The mean flux density for each source is computed by averaging over the entire observing epoch, with each point inversely weighted by the estimated measurement variance. For our final results, we used only the 30–32 GHz band, which we take to have a nominal center frequency of 31.0 GH. This is the center of the CBI observing band and corresponds closely to the most sensitive channel of the GBT receiver, readily allowing direct comparisons.

4.3. GBT Observations

Test observations of the CCB and 26–40 GHz receiver on the GBT were conducted in 2005 November and December, and 2006 January; these observations confirmed lab measurements of the system performance. The science observations ran from 2006 February 2 through 2006 May 7. We collected 3198 observations of 3040 NVSS sources; after the data filtering described below, 1567 observations of 1490 sources remain in the final data set.

For these observations, we developed an "On-the-Fly Nod" variant of the double-differencing technique described in

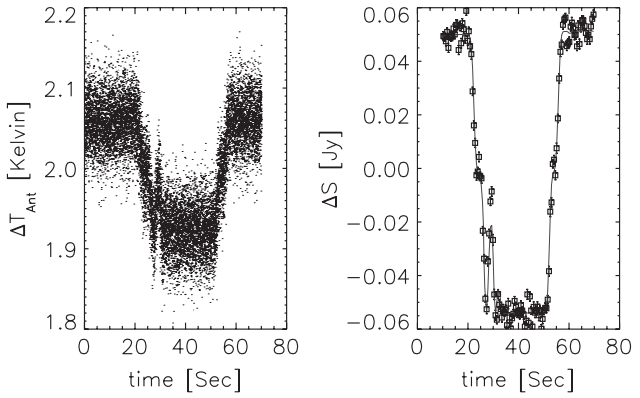

Figure 4. Measurement of steep-spectrum source 085328 − 0341 at 31.25 GHz. The left-hand plot shows the individual 5 ms beam-switched integration calibrated via the noise diode to antenna temperature. The right-hand plot shows the individual beam-switched integrations averaged into 0.5 s measurements with error bars given by the internal scatter of each 0.5 s measurement and flux density calibrated via 3c286; here, the initial 10 s settle period has been excised. The remaining data illustrate the symmetric A/B/B/A nod pattern in which the source was placed in the two beams of the receiver. The solid line in the right panel shows the template fit (Equation (4)).

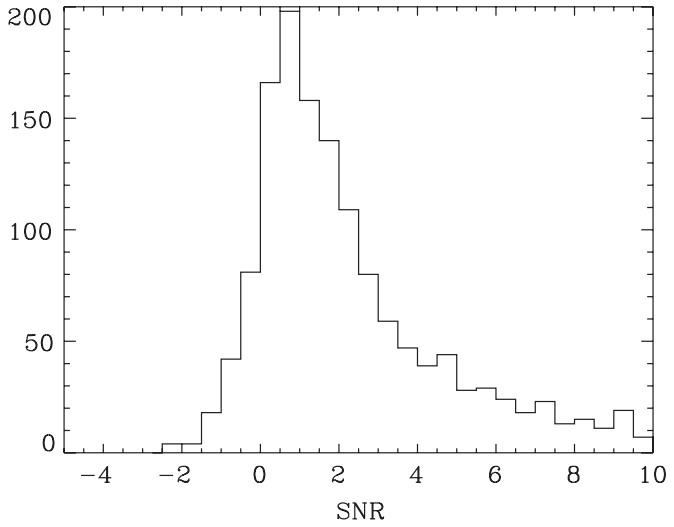

Figure 5. Distribution of the signal-to-noise ratio for the measurements in the GBT survey. Compare with blank-field measurements in Figure 6.

Section 4.1 and Readhead et al. (1989). With this technique data are collected continuously through the entire observation, including the slews between beams. The recorded (10 Hz) antenna positions are used with the target source coordinates to construct a template beam-switched signal which is fitted to the differenced data. This approach minimizes scan-start overheads and provides a conveniently continuous datastream for each source; it also allows us to carefully account for imperfect source acquisition and settling times offline. An example observation of a bright source is shown in Figure 4. A typical feature is the spike at $\sim$ 30 s. In actuality, the spike is a dip in the source signal coming from the negative beam, and arises from stiction in the telescope servo resulting in overshooting the source slightly when slewing in one direction. Since this overshoot was recorded by the antenna position encoders, it is reflected in the template model and has minimal effect on our observations, particularly of our much weaker science sources. The on-source dwell time in each phase was 10 s; there was a 10 s slew between A and B phases. A 10 s settle was also allowed at the start of each scan in order to allow possible GBT feedarm vibrations (occasionally excited by the servo system at the start of a scan) to settle, but this was never seen to be an issue in our frequent bright-source calibration checks. The average slew time between program sources was 20 s, for an average total elapsed time per-source measurement of 90 s. During the nod measurement, the detected RF power in each of 16 channels was recorded at 200 Hz by the CCB.

During daylight, the GBT pointing and focus was checked every half-hour on a nearby bright source ($S_{31\,\mathrm{GHz}} > 500$ mJy); at night, this was relaxed to every 45 minutes. During each pointing and focus check, a nod observation was also collected to monitor intraday stability of our measurements. To monitor interday repeatability of our calibration, we selected a steep-spectrum (NVSS/OVRO) source near each CBI field as well and measured it at least once per observing session.

4.4. GBT Data Reduction

While the GBT observations are similar to the OVRO observations, several important differences led to a different approach to reducing the data. First, substantially less "data reduction" (averaging) was performed by the online data acquisition system, enabling preservation of more data for offline diagnostics. Second, the typical signal to noise in a GBT observation was of order unity owing to the higher sensitivity of the telescope—see Figure 5. Finally, the data set was substantially smaller, less than a week in total in contrast to several years of OVRO observations.

The CCB data were first averaged from 5 ms to 0.5 s integrations $d(t_i)$ and each integration was assigned an error estimate based on the internal scatter of the beam-switched 5 ms integrations. The 10 Hz recorded antenna positions were interpolated onto the same time sampling as the CCB data resulting in a time series of positions $\vec{x}_j(t_i) \equiv \vec{x}_{j,i}$ for a given feed indexed by $j = 1, 2$ for a given observation. The beam locations on the sky and measured GBT beam pattern B as a function of frequency were used to compute the expected beam-switched response of the receiver to a point source of flux density s_o at the location of the source of interest, $\vec{x}_o$

$$d_i = s_o \times [B(|\vec{x}_{1,i} - \vec{x}_o|) - B(|\vec{x}_{2,i} - \vec{x}_o|)] + \langle d_i \rangle + \frac{dd_i}{dt}, \quad (4)$$

where the difference in square brackets comes about due to the beam switching. The last two terms are mean (radiometric offset) and gradient terms allowed in the fit and which, due to the symmetry of the nod pattern, are approximately orthogonal to the source flux density parameter s_o. This template was fitted directly to the beam-switched data—refer again to Figure 4 for an example. The χ^2_ν of the fit is a good diagnostic of data quality; for sources weaker than 10 mJy, χ^2_ν was close to unity under good conditions. As weather conditions degrade, our simple model fails resulting in appreciable increase of the χ^2_ν. For sources brighter than $\sim$ 10 mJy, χ^2_ν rarely approached unity even under excellent observing conditions due to imperfections in the beam model and residual pointing errors. These observations required separate consideration in χ^2_ν-based filters.

Using observations of 3C286 throughout the observing campaign a single mean calibration, referenced to the WMAP-5 Jupiter-temperature scale described in Section 4.1, was determined for each channel. For the final processing, this calibration was applied to the individual detector timestreams and all timestreams for a given frequency were averaged in the time domain before performing the source flux density fit of

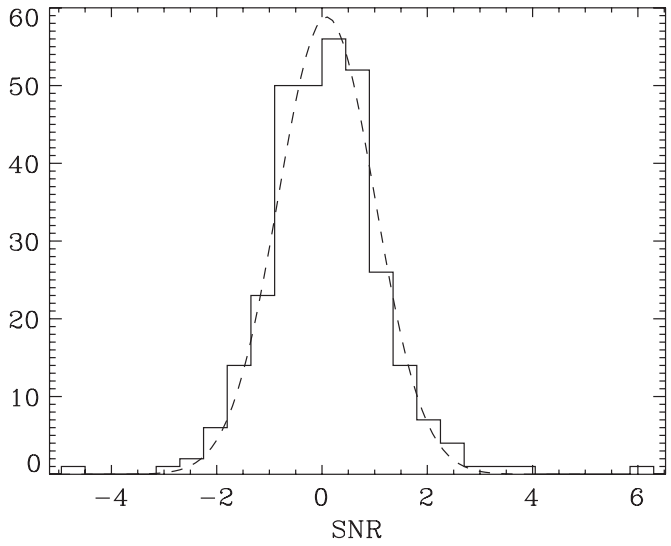

Figure 6. Distribution of blank-field measurements divided by their individual measurement noises estimated by Equation (5). The dashed line shows the best-fitting Gaussian which has $\sigma = 0.91$, close to the expected value of unity which would be obtained for perfectly estimated Gaussian noise; the noise values themselves varied by a factor of 4. Compare to the corresponding distribution of measurements that targeted NVSS sources in the survey, Figure 5.

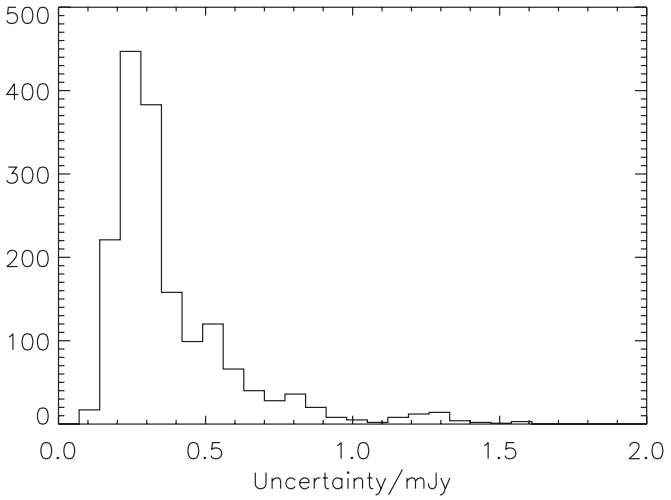

Figure 7. Distribution of rms measurement errors in the GBT survey, estimated as described in the text.

Equation (4). This ensured that noise fluctuations correlated between feeds or polarizations were correctly accounted for in the noise estimate that follows.

Repeated observations of bright, steep-spectrum sources near our fields (also of fainter steep-spectrum sources) provided a check on the validity of our pointing filters. We found that the accuracy of our calibration for an individual source is 10% (rms) at 31 GHz, dominated by uncertainties in the GBT pointing.

Since the signal to noise in a typical 70-s GBT observation was of order unity, we could not straightforwardly compute the noise in our data from the scatter of the measurements (i.e., the fitted values of the source flux densities s_o) as we did for the OVRO measurements. Instead, we formed alternate combinations of the individual segments of the symmetric Nod procedure to quantify the photometric stability of the measurement. Designating the average value of integrations within individual segments of the nod by A_1, B_1, B_2, and A_2, then $\Delta A = A_1 - A_2$ is a source-signal-free combination measuring to the photometric fluctuation over 50 s, and $\Delta B = B_1 - B_2$ is a source-signal-free combination measuring the photometric fluctuation over 10 s. From test observations of blank patches of sky under a wide range of conditions, we found that the average (over some window of many observations) of the rms of ΔA and ΔB gave an estimate of the rms of the measured flux density values s_o accurate to within 10%. Note that since both A and B respond to time gradients of the beam-switched signal, whereas the fitted source flux density (s_o in Equation (4)) does not, we might expect them to slightly overestimate the noise. To improve the robustness of this noise measure, we computed the mean absolute deviation (MnAD) of ΔA and ΔB rather than the rms and renormalize to a Gaussian equivalent (MnAD $= \sqrt{2/\pi}\sigma_g$); we chose the somewhat less robust but lower variance MnAD over the MedAD used in Section 4.2 because outliers are a lesser concern for the signal-free estimators ΔA and ΔB than in the flux density measurements themselves. For each measurement, we computed these quantities in a 1 hr buffer centered on the observation in question. With the appropriate normalization constants, derived in the white-noise limit, this approach gave a noise estimate

$$N(t_i) = \frac{\sqrt{\pi}}{8}[\mathrm{MnAD}(\Delta A) + \mathrm{MnAD}(\Delta B)] \quad (5)$$

(where the MnADs were computed from all observations within plus or minus a half-hour of t_i) close to the rms that signal-free nod measurements would have given under the same conditions. The data from the blank-field test observations are shown in Figure 6, normalized by the individual estimated measurement errors. The actual per-measurement noises varied by a factor of 4. The dispersion in the noise-normalized data is $\sigma = 0.91$, acceptably close to the $\sigma = 1.0$ which would result from perfectly measured Gaussian noise. As expected the noise was slightly overestimated due to the presence of radiometric gradients.

The mean noise level in the GBT data which pass the data filters described below is 390 μJy. The distribution is shown in Figure 7.

The main time-variable systematics that affect our data were departures from good photometric conditions caused by atmospheric clouds and water vapor and telescope pointing and focus. A series of filters excised compromised observations. To identify periods of poor photometry, we computed the median χ^2_ν in sliding 1 hr buffers—excluding measurements brighter than 10 mJy—and rejected observations for which this value exceeds 1.4. To catch rare isolated glitches, individual observations with $\chi^2_\nu > 1.4$ were also rejected *unless* the fitted flux density exceeded 10 mJy. In this case, the observation was inspected manually; all passed inspection so were retained.

In the course of commissioning and operations, the pointing and focus performance of the GBT was extensively characterized, with results summarized by Condon (2003) and Balser et al. (2006). Under calm conditions (winds under 3.0 m s^{-1}), the observed rms in the radial pointing offset is 2.″7, corresponding to less than 5% loss of peak signal for the GBT's 24″ (FWHM) beam at 31 GHz. When the wind speed is greater than a few meters per second, the GBT pointing performance degrades, principally due to excitation of feedarm vibrations; up to 4.0 m s^{-1}, the pointing accuracy is still acceptable for 31 GHz observations. We rejected individual observations with mean wind speeds over 3 m s^{-1}; we also reject individual observations with peak wind speeds over 5 m s^{-1}. Every half-hour

Table 1
Summary of GBT Data Filters

Filter	Criterion	Fraction of Data Passed (%)
Wind	Max < 5.0 m s^{-1}, mean < 3.0 m s^{-1}	79
$\langle\chi^2_\nu\rangle$	< 1.4	54
Pointing and focus updates	Within 30 (day) or 45 (night) minutes	86
Total		39

Note. We show the fraction of the total data set that passes each individual filter; since there are correlations between the filtered variables the filters are not statistically independent.

(during the day) to 45 minutes (at night), the telescope pointing and focus was updated from observations of a nearby calibrator. Science program observations that are not preceded by a successful peak and focus correction within these periods of time are also rejected. There were no GBT data for which the Sun or the Moon were closer than 10° away. The data filters are summarized in Table 1.

To check the effectiveness of our pointing update criteria, we considered the ratio r of measured flux density in the 38 GHz band to that measured in the 31 GHz band for all sources detected at 4σ or greater. The flux density measured in the high-frequency band will fall more for a given pointing offset than will the lower frequency band. For the data set as a whole $r = 0.84 \pm 0.03$, where the uncertainty is the error in the mean assuming Gaussian statistics from the rms of the distribution. From the spectral-index analysis of Section 5.1, we calculated an expected $r = 0.83 \pm 0.04$, where the error bar in this case is the rms of the distribution (indicating its intrinsic width) predicted by our maximum-likelihood spectral-index distribution under the assumption of a single power-law extrapolation. Note that selecting 4σ detections will bias r slightly high relative to the full distribution. Splitting the data into two halves based on the time since the last pointing calibration, the data with more recent corrections have an average flux density ratio of 0.84, while data with less-fresh pointing corrections have an average flux density ratio of 0.83, indicating no significant change in the telescope pointing between pointing checks. Similarly, the daytime data have $r = 0.83$ and the nighttime data $r = 0.84$, indicating that on average the thermal effects prevalent during the day do not significantly affect the telescope pointing. The $\Delta r = 0.01$ differences seen correspond to average radial pointing offsets of $2''$ or 2% gain effects; a 10% loss in gain overall, if caused by a pointing offset, would correspond to $\Delta r = 0.05$ (a $4\farcs6$ radial offset). Note that this test is sensitive to any errors which causes relative changes in observed power across the receiver band. For instance, variations in the Ruze-equivalent rms deviation of the telescope surface from a perfect paraboloid scale as $\exp(-(4\pi\epsilon/\lambda)^2)$ and will also affect the 38 GHz channel more than the 31 GHz channel.

To further check the accuracy of our noise estimate, we made use of the fact that in the course of the survey 50 weak ($S_{31} < 15$ mJy) sources were observed more than once; we selected weak sources in order that the effect of gain errors, which can be correlated between observations, not be a dominant effect. In all, there are 122 such observations. Subtracting the per-source means from each, we calculate a $\chi^2_\nu = 0.95$ for $\nu = 72$. The probability to exceed this by chance is 59%.

4.5. The Effect of Finite Source Size

While most radio sources are compact compared to the GBT and OVRO beams, a handful are sufficiently extended that flux density is lost in targeted observations. On angular scales at which the GBT begins to lose flux density ($\sim 10''$) most of the extended emission seen in extragalactic sources originates in radio jets with a synchrotron spectrum $\propto \nu^{-0.6}$ to ν^{-1} (Laing & Peacock 1980; Dennett-Thorpe et al. 1999); the 31 GHz emission is dominated by the compact, flatter-spectrum cores. Consider, for example, that the NVSS at 1.4 GHz, with a $45''$ (FWHM) beam find 20% of sources to be resolved, while 9C at 15 GHz, with a $25''$ FWHM beam, finds only 9% of sources to be detectably resolved (E. M. Waldram 2008, private communication). Consequently, we expect that most of the flux density in the 31 GHz sky will be in compact sources which are accurately measured by the GBT.

To test for lost flux in the data set, NVSS sources with useful GBT measurements were divided into two groups—those resolved by NVSS and those not resolved by NVSS—and from these groups we constructed two CBI visibility templates (actually, gridded estimator templates). We fit for a scale factor $S_{\rm CBI} = f \times S_{\rm GBT}$ for each template using the CBI visibility data in aggregate. For sources unresolved by NVSS, we find $f = 0.96 \pm 0.04$, indicating that there is no systematic bias between the flux density scales and that there is no significant degree of source extension that is not detected by NVSS. Fitting for a CBI/GBT scale factor using only the NVSS-*resolved* sources yields $f = 1.18 \pm 0.10$. The larger error bar in this is consistent with the (smaller) number of extended sources in comparison to the number of compact sources in the NVSS catalog.

We found that excising the extended sources from the spectral-index analysis of Section 5.1 did not significantly change the spectral-index probability density function (PDF) or final result for the residual source correction. This is consistent with the expectation that the 31 GHz sky variance is dominated by the flat, compact sources.

4.6. Confusion

Since the angular resolution of the GBT and, especially, OVRO surveys are comparatively low ($24''$ and $1\farcm3$, respectively) chance superpositions of radio sources occasionally occur and must be considered. To assess the effects of source confusion, we combined the OVRO and GBT catalogs, giving precedence to GBT measurements where present, and selected 3σ or greater detections. To this, we added the NVSS sources with 1.4 GHz flux densities >3.4 mJy and multiplied their flux densities by 0.1 (the mean ratio of S_{31} to $S_{1.4}$ determined from the maximum-likelihood analysis of Section 5.1), thereby obtaining our best estimate of the point-source 31 GHz sky in the regions observed. We call this our "reference" catalog.

Using the reference catalog, we scanned the full set of OVRO observations and identified those for which the sum of the absolute values of beam-weighted confusing source flux densities in the reference catalog amounts to more than half the measurement error for that source. This amounts to 1.3%

Table 2
Excerpt of OVRO 40 m Survey Results

Name	R.A./J2000	Decl./J2000	S30	E(S30)	S(1.4)	E(S1.4)	Maj	Min	D	C
085057-0150	08 50 57.06	−01 50 38.6	5.30	1.91	46.90	1.50	0.0	0.0		
085101-0509	08 51 01.80	−05 09 52.9	3.00	3.40	36.30	1.20	0.0	0.0		
085103-0303	08 51 03.94	−03 03 35.5	2.00	2.20	17.80	1.40	71.4	0.0		
085118-0419	08 51 18.93	−04 19 10.3	−3.13	2.81	62.70	2.30	15.3	0.0	*	
085121-0418	08 51 21.49	−04 18 25.7	11.74	2.79	66.00	2.40	45.5	0.0	*	*
085127-0156	08 51 27.01	−01 56 09.3	4.00	5.00	18.70	1.00	22.7	0.0		
085130-0155	08 51 30.58	−01 55 49.4	−4.30	3.80	22.70	0.80	0.0	0.0		
085135-0150	08 51 35.60	−01 50 44.9	5.80	2.71	55.20	1.70	0.0	0.0		
085137-0405	08 51 37.67	−04 05 00.7	3.40	3.30	27.40	0.90	0.0	0.0		
085138-0451	08 51 38.97	−04 51 23.8	14.20	3.25	78.40	2.40	0.0	0.0	*	
085141-0424	08 51 41.73	−04 24 35.6	2.80	2.10	13.70	0.60	0.0	0.0		
085149-0314	08 51 49.11	−03 14 57.0	0.70	2.50	81.40	2.90	29.8	0.0		
085157-0408	08 51 57.40	−04 08 01.2	−0.10	1.80	17.30	0.70	0.0	0.0		

Notes. Positions and 1.4 GHz flux densities are from NVSS. Columns are NVSS name, right ascension (J2000), declination (J2000), 31 GHz flux density and uncertainty in mJy, NVSS integrated flux density and uncertainty, NVSS major axis in arcseconds (0.0 indicates no detected size), and NVSS minor axis in arcseconds. A flag in the "D" column indicates a 4σ detection, and a flag in the "C" column indicates that a confusion correction has been performed by the method described in the text.

(This table is available in its entirety in a machine-readable form in the online journal. A portion is shown here for guidance regarding its form and content.)

Table 3
Excerpt of GBT 31 GHz Survey Results

Name	R.A./J2000	Decl./J2000	S30	E(S30)	S(1.4)	E(S1.4)	Maj	Min	D	C
024033-0430	02 40 33.46	−04 30 00.5	0.17	0.30	3.60	0.60	0.0	0.0		
024033-0432	02 40 33.53	−04 32 47.5	0.37	0.32	5.50	0.50	0.0	0.0		
024038-0425	02 40 38.89	−04 25 54.5	0.81	0.32	4.00	0.50	0.0	0.0		
024055-0428	02 40 55.18	−04 28 36.4	0.34	0.30	4.50	0.50	0.0	0.0		
024108-0422	02 41 08.83	−04 22 51.4	5.32	0.61	6.90	0.50	0.0	0.0	*	
024111-0425	02 41 11.61	−04 25 21.4	1.23	0.32	26.80	0.90	0.0	0.0	*	
024119-0421	02 41 19.39	−04 21 44.4	2.71	0.43	17.20	0.70	0.0	0.0	*	
024129-0003	02 41 29.53	−00 03 27.4	−2.40	1.19	4.70	0.50	0.0	0.0		
024137-0039	02 41 37.85	−00 39 19.4	0.56	0.61	14.60	0.60	0.0	0.0		
024144-0416	02 41 44.17	−04 16 48.0	5.88	0.67	84.50	3.30	32.6	16.5	*	
024146-0025	02 41 46.15	−00 25 01.7	0.89	0.61	5.70	0.50	0.0	0.0		
024153-0105	02 41 53.70	−01 05 43.3	0.15	0.24	3.40	0.50	0.0	0.0		
024204-0053	02 42 04.56	−00 53 33.7	0.26	0.24	5.60	0.50	0.0	0.0		

Notes. Columns are as in Table 2.

(This table is available in its entirety in a machine-readable form in the online journal. A portion is shown here for guidance regarding its form and content.)

of the OVRO catalog. For these measurements, a correction is calculated using the procedure described in Appendix A.

Owing to the smaller beam size and beam throw, the level of source confusion in the GBT data was much lower. Using the same criteria only two observations were significantly confused; for these sources the correction described in Appendix A was also performed.

4.7. Source Catalogs

The full set of OVRO observations is presented in Table 2, and the GBT survey results are presented in Table 3. Reported error bars include a 10% and 5% rms gain uncertainty for GBT and OVRO measurements, respectively. Sources detected at greater than 4σ at 31 GHz are marked; for this calculation, the random gain uncertainty is excluded. In all 3165 sources were observed. The GBT catalog contains 1490 sources. Of the 2315 useful OVRO observations many of the non-detections (and a few detections) are superceded by more sensitive GBT observations; the OVRO catalog therefore contains data on 1675 sources. The detection rate of the OVRO measurements was 11%, and that of the GBT measurements 25%. In all, 18% of sources were detected at 31 GHz.

Also included in the table are the 1.4 GHz flux densities, source sizes from the NVSS catalog, flags to indicate 4σ detections, and flags to indicate which observations have been corrected for the effects of source confusion in either the main or reference beams.

The catalogs presented here are based on the processing described in Sections 4.2 and 4.4. The analysis (Sections 5.2 and 5.3) used an earlier processing with slightly less strict filters. The total number of sources in this catalog was 3562. The spectral-index distributions obtained from these two versions of the source lists are consistent.

5. INTERPRETATION

5.1. Spectral-index Distribution from GBT, OVRO, and NVSS Data

In order to determine the contribution of radio sources below the NVSS completeness limit to the sky variance measured by 31 GHz CMB experiments such as the CBI, it is necessary to understand the 1.4–31 GHz spectral-index distribution—or equivalently, the PDF of S_{31} given $S_{1.4}$. The data from the survey presented in this paper are the best currently available for this

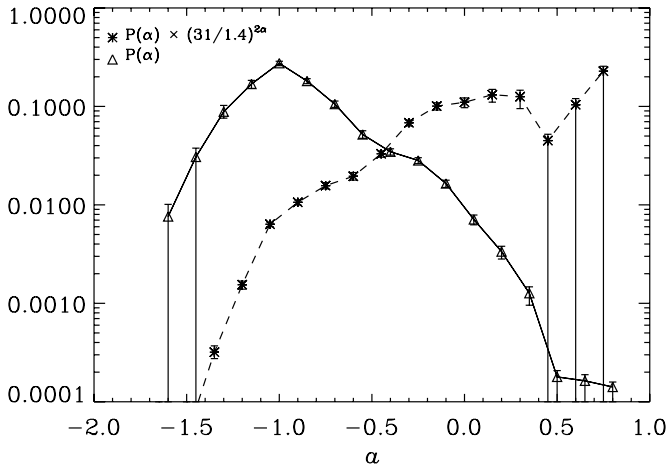

Figure 8. 1.4–31 GHz spectral-index distribution determined from GBT, OVRO, and NVSS data. Error bars are the one-parameter marginalized 1σ uncertainties for the individual points parameterizing the spectral-index PDF. Also shown is the PDF weighted by $(31/1.4)^{2\alpha}$, which is proportional to the contribution that sources of a given α make to the variance of the 31 GHz sky intensity.

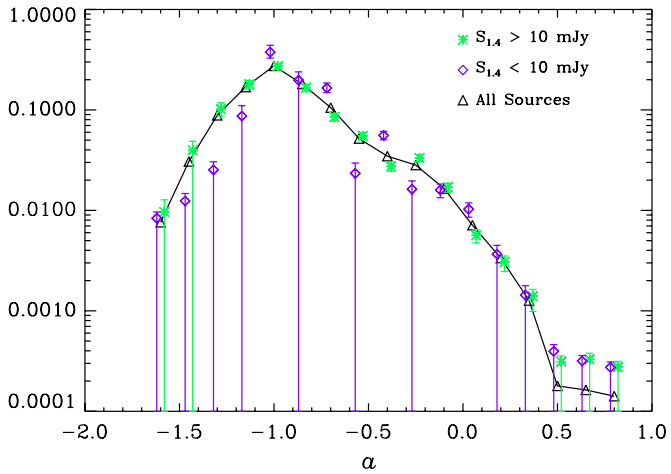

Figure 9. Spectral index from 1.4 to 31 GHz determined from bright ($S_{1.4}$ > 10 mJy) and faint ($S_{1.4}$ < 10 mJy) subsets of the full data set. We also show the spectral-index distribution from the full data set.

(A color version of this figure is available in the online journal.)

purpose. Since sources detected at 31 GHz are preferentially flat spectrum, it is necessary to include non-detections in this analysis to obtain an unbiased result. Because we know the low-frequency flux densities of these sources and the 31 GHz measurement noise, these non-detected sources will impose constraints on the spectral-index distribution. We adopted a Bayesian maximum-likelihood approach.

We wish to find the spectral-index distribution that maximizes the likelihood of measuring the observed 31 GHz flux densities given their observed 1.4 GHz NVSS flux densities. The general form of the likelihood of measuring 31 GHz flux density $S_{31,\mathrm{obs}}$ given 1.4 GHz flux density $S_{1.4,\mathrm{obs}}$ is

$$P(S_{31,\mathrm{obs}}|S_{1.4,\mathrm{obs}}) = \int\int P(S_{31,\mathrm{obs}}|S_{31,T})P(S_{31,T}|S_{1.4,T}) \times P(S_{1.4,T}|S_{1.4,\mathrm{obs}})dS_{31,T}dS_{1.4,T} \quad (6)$$

integrating over the unknown values of the "True" flux densities $S_{31,T}$ and $S_{1.4,T}$, and with the (unknown) 1.4–31 GHz spectral-index function $P(S_{31,T}|S_{1.4,T})$. We parameterized $\frac{S_{31,T}}{S_{1.4,T}}$ with a set of $N_{\mathrm{bin}} = 17$ points in the frequency spectral index α evenly spaced between $\alpha = -1.6$ and $\alpha = +1$. Appendix B contains a more detailed discussion of the evaluation of this likelihood function.

To measure the PDF and its uncertainty, we used the publicly available Markov-Chain Monte Carlo (MCMC) code COSMOMC (Lewis & Bridle 2002) adapted for use with a generic likelihood function. The MCMC algorithm draws samples from a multi-dimensional parameter space, in this case the space of N_{bin} parameters representing the spectral-index distribution, with a specified distribution, in this case the likelihood of the parameters given the data. This procedure permits easy evaluation of the uncertainties and covariances in parameters of interest (the spectral-index distribution); it also makes evaluating the uncertainties and covariances in functions of these parameters straightforward (e.g., Section 5.2).

We show the marginalized posterior distributions of the parameters of the spectral-index PDF in Figure 8. This is our best description of 1.4–31 GHz source spectral indices. This figure also shows the spectral-index distribution weighted by $(31/1.4)^{2\alpha}$, and therefore proportional to the variance in 31 sky brightness that residual point sources of a given spectral index contribute. Table 4 summarizes the results in binned form, calculated from 100,000 samples from the MCMC chains. We found that the mean 31–1.4 GHz flux density ratio is 0.111 ± 0.003, corresponding to a spectral index -0.71 ± 0.01. The distribution is heavily skewed toward steep spectral indices with a long tail in the flat direction, resulting in a *mean spectral index* steeper than the value $\alpha = -0.71$ that corresponds to the mean flux density ratio ($\langle\alpha\rangle = -0.92^{+0.29}_{-0.30}$, 68.5% confidence interval). 9.0% ± 0.8% of sources have spectral indices flatter than $\alpha > -0.5$ and 1.2% ± 0.2% have inverted spectral indices, $\alpha > 0$.

To check the important assumption that the spectral index does not change as a function of 1.4 GHz flux density, we split the sample into $S_{1.4} > 10$ mJy and $S_{1.4} < 10$ mJy subsamples and estimated the spectral-index distribution for each of the bright and faint samples separately, with results shown in Figure 9. At low flux densities, the faint subsample provided little constraint on the spectrally steep end of the distribution, reflected by large error bars in that regime. The consistency of the subsamples supports the assumption that the spectral-index distribution is constant over the range of flux densities of interest. To further assess the robustness of our conclusions, we re-ran the spectral-index distribution chains varying the assumed noise level of the OVRO and GBT data by ±20% and excised potentially confused sources. The results, along with the nominal case, are summarized in Table 5. We show the mean spectral index and its rms, the fraction of sources with flat our rising spectra, the mean 31–1.4 GHz flux density ratio, and the mean-square flux density ratio, which is more indicative of the variance of the source population.

5.2. 31 GHz Source Counts

We estimated the 31 GHz counts by drawing flux densities between 50 μJy and 1 Jy from the Hopkins et al. 1.4 GHz counts and extrapolating them to 31 GHz with samples from our 1.4 to 31 GHz PDF. Over the range 1 mJy < S_{31} < 15 mJy, the counts follow a power law $dN/dS \propto S_{31}^{-1.8}$, with a normalization at 1 mJy of $S^{5/2}\,dN/dS = 1.18 \pm 0.05$ Jy$^{-1.5}$ sr^{-1}. Directly summing the simulated source populations gives an integrated

Table 4
The 1.4–31 GHz Spectral-Index Distribution Determined from GBT, OVRO, and NVSS Data

Spectral Index	f/%
−1.60	< 1.8
−1.45	3.1 ± 1.6
−1.30	8.8 ± 2.8
−1.15	16.9 ± 3.3
−1.0	27.4 ± 3.0
−0.85	18.1 ± 2.4
−0.7	10.6 ± 1.6
−0.55	5.2 ± 1.0
−0.40	3.5 ± 0.6
−0.25	2.8 ± 0.4
−0.10	1.6 ± 0.3
0.05	0.7 ± 0.2
0.20	0.3 ± 0.1
0.35	0.1 ± 0.1
0.50	< 0.05
0.65	< 0.05
0.80	< 0.04

Note. For bins consistent with zero at $1\sigma, 2\sigma$ upper limits computed from the likelihood function are listed.

Table 5
Results of Tests of the Spectral-index Distribution Estimate

Test	Noise ×0.8	Nominal	Noise ×1.2
$f_{\alpha \geqslant 0.0}$	$1.24\% \pm 0.15\%$	$1.17\% \pm 0.15\%$	$0.92\% \pm 0.18\%$
$\langle S_{31}/S_{1.4} \rangle$	0.117	0.111	0.101
$\langle (S_{31}/S_{1.4})^2 \rangle$	0.099	0.092	0.084
$\langle \alpha \rangle$	−0.911	−0.917	−0.925
$\langle \sigma_\alpha \rangle$	0.336	0.311	0.292

Notes. We show the fraction of rising spectrum sources, the mean flux density ratio (1.4–31 GHz), the mean of the square of the flux density ratio (which is directly relevant to the residual source variance), and the mean spectral index for a range of perturbed GBT and OVRO noise levels, and for the case where all measurements potentially affected by confusion are excised.

source count of

$$N(> S_{31}) = (16.7 \pm 1.7) \times (S_{31}/1\ \mathrm{mJy})^{-0.80 \pm 0.07}\ \mathrm{deg}^{-2}. \quad (7)$$

As shown in Figure 10, our 31 GHz counts compare favorably with other measurements (Mason et al. 2003; Cleary et al. 2005; Kovac et al. 2002). We can apply this procedure over an arbitrary range of flux densities but it is only valid over the range that our spectral-index PDF is valid. Based on the observed 31–1.4 GHz PDF, we estimate that the potentially distinct source populations at $S_{1.4} < 1$ mJy and $S_{1.4} > 100$ mJy could contribute 10% or more of the sources at $S_{31} < 1$ mJy and $S_{31} > 4$ mJy, respectively, so take this to define the range over which our counts are valid. These potential contributions to the counts also set the uncertainty in the power-law slope. Error bars were checked using the set of MCMC-sampled spectral-index PDFs, but are dominated by the assumed 10% systematic uncertainty. However, the agreement with models and data is good over a much wider range of flux densities, suggesting that the change of the source spectral indices is not especially strong. The GBT counts have a similar slope to the model of de Zotti et al. (2005), although the normalization of the GBT counts is 15% lower in the 1–10 mJy range. The Toffolatti et al. (1998) counts are substantially higher than both in this range. Below 0.3 mJy,

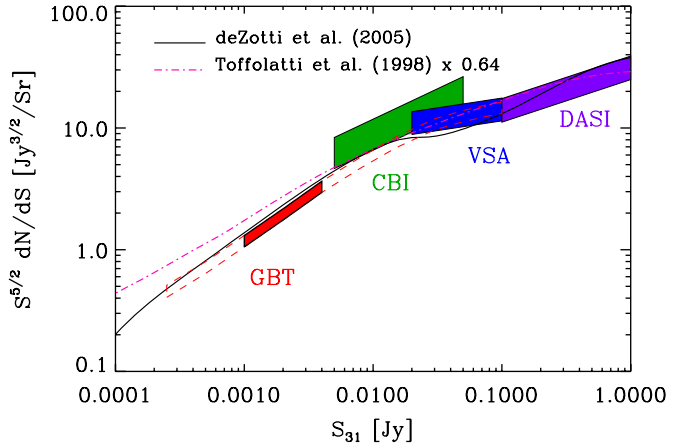

Figure 10. Summary of 31 GHz source count measurements and models. CBI results are from Mason et al. (2003), VSA results from Cleary et al. (2005), and DASI results from Kovac et al. (2002). All data are at 31 GHz except for VSA, which is at 33 GHz. Also shown is the Toffolatti et al. (1998) 31 GHz model scaled down by a factor of 0.64 and the de Zotti et al. (2005) 33 GHz model. The derivation of the GBT error box is described in the text; the solid red box shows our best estimate of the counts, valid over 1 mJy $< S_{30} <$ 4 mJy and the red dashed line shows the result over the full range 0.25 mJy $< S_{30} <$ 100 mJy. Other experiments' errors are taken from the Poisson error in the count normalization.

(A color version of this figure is available in the online journal.)

the 31 GHz counts in our model show a weak turn-up due to the submillijansky population but the precise location and magnitude of this turn-up depend on the assumed spectra of these sources (see Section 5.3.2).

5.3. The Effect of Unidentified Sources on CBI Measurements

5.3.1. Simulations

Point sources are the largest astrophysical foreground in the CBI data, and are especially critical at high-ℓ. An accompanying paper (Sievers et al. 2009) presents the power spectrum from five years of CBI observations. We have used the results of GBT and OVRO 40 m measurements presented here to quantify the impact of discrete sources on the power spectrum. As discussed in Section 1, there are two distinct classes of sources to be treated: those which are individually known and identified from imaging surveys (NVSS) and sources in our fields not detected in any survey, but expected to be present based on source counts extending below the survey detection limits in other fields. Very conservatively, all known sources are projected out of the CBI data set; the efficacy of this procedure is quantified in Sievers et al. (2009). Our task, and the fundamental aim of this paper, is to quantify the statistical contribution of the fainter sources. This population is a *low-frequency selected population* (sources below the NVSS detection threshold), and we must calculate the variance of its sky brightness at 31 GHz.

To do this, we undertook an extensive suite of simulations. We created realistically constrained realizations of the sub-NVSS populations and ran these realizations through the full CBI power spectrum pipeline; the procedure is schematically illustrated in Figure 11. We first drew 1.4 GHz populations down to 0.2 mJy using a power-law fit to the FIRST counts (White et al. 1997) between 2 and 100 mJy, representing the dominant contribution of mJy-level active galactic nucleus (AGN). The contribution of sources below 1 mJy at 1.4 GHz, which likely have different spectral indices than the mJy AGN, is

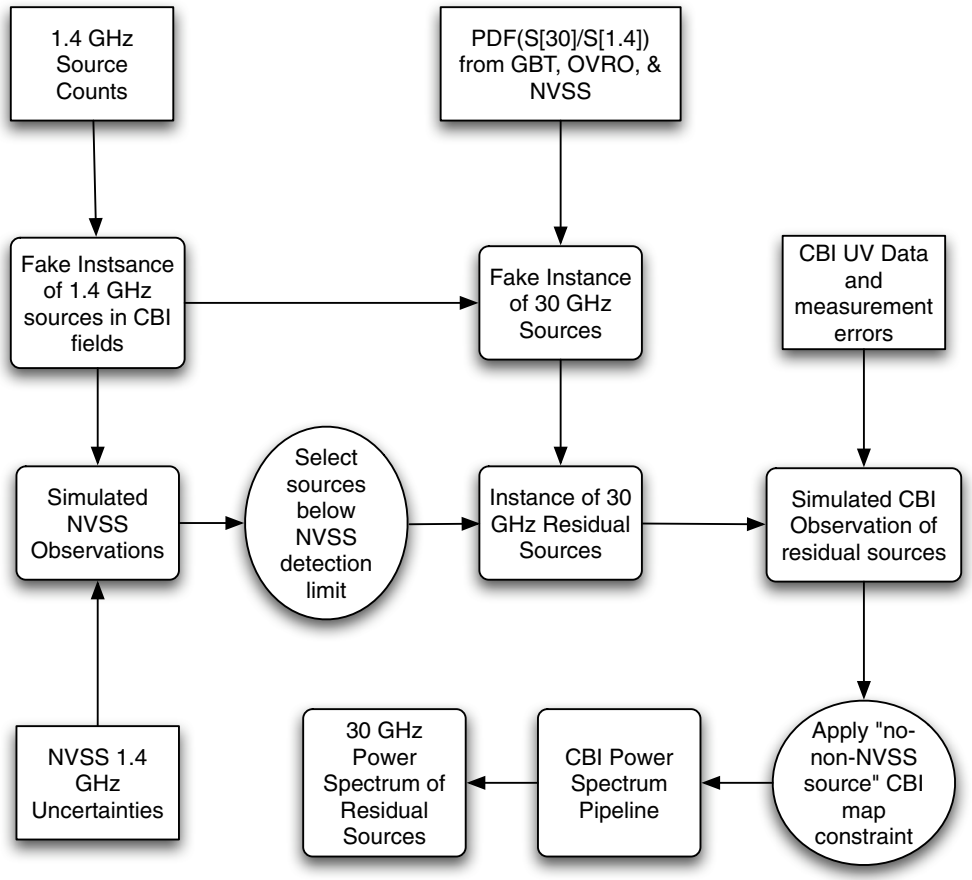

Figure 11. Schematic of the simulation pipeline we use to estimate the distribution of residual source power in the CBI power spectrum.

considered separately in Section 5.3.2. We then simulated NVSS observations of these source realizations, adding Gaussian noise typical of the NVSS thermal noise (0.6 mJy). Any source that has an observed (noisy) flux density greater than our NVSS projection threshold of 3.4 mJy was then removed, leaving a realistic population of 1.4 GHz sources that would not have appeared in NVSS. Sources on the power-law dN/dS with $S_{1.4} < 0.2$ mJy, which we do not simulate, will contribute $< 2\%$ of the power. We then drew one 1.4–31 GHz spectral-index distribution from the Markov chains in Section 5.1, with the assumption that the spectral-index distribution is independent of 1.4 GHz flux density, and assigned each source a spectral index drawn from the distribution. The signal from these faint-source realizations was added to CMB+noise simulations of the CBI data set.

An additional constraint came from the fact that the CBI maps, at a typical 5σ level of $S_{31} = 20$ mJy, shows no sources that are not present in NVSS. This limits the strongly inverted-spectrum tail of the spectral-index distribution. At the NVSS lower flux limit roughly one in three CBI synthesized beams ($\sim 5'$ FWHM) has an NVSS source in it, so at the fainter 1.4 GHz flux densities characteristic of the residual sources chance superpositions will be common. Such a blend would appear to the CBI as a single orphan source. Therefore the absence of non-NVSS sources in the 31 GHz CBI maps also constrained the abundance of more modestly inverted-spectrum sources *for the particular realization of sources present in the CBI fields*. In this analysis we found that the latter was the more important constraint.

To fold in this constraint, we imaged each simulation and searched it for "orphan" sources using the method described in L. Weintraub et al. (2010, in preparation), and rejected any realization where such a source is found. There were a 4–5σ features in the CBI maps that were marginally inconsistent with being associatable with an NVSS source(s). We followed each of these up with the GBT and do not detect them, implying that they are probably noise fluctuations. It is still possible that these fluctuations were chance superpositions of multiple faint sources in the same CBI beam. The GBT could miss such a superposition if no individual source falls within the GBT's much-smaller beam when pointed at the effective emission center. To account for this possibility, we carried out mock GBT observations on fluctuations in the simulated maps that were classified as orphan sources, and do *not* reject any simulation based on map fluctuations that would not have been seen by the GBT. This gave us a set of simulated source catalogs that are consistent with the observed 1.4–31 GHz spectral-index distribution and the fact that CBI detects no orphan 31 GHz sources.

We created 500 simulations, 250 for each of the binnings in Section 5.1, and subjected them to the map test described above. In 215 of the 500 (the "clean" simulations), no orphan sources are detected in the simulated CBI maps. In 285 of them (the "dirty" simulations), one or more orphan source is detected. We take the visibilities from the source simulations and run them through the full CBI power spectrum pipeline, fitting an ℓ^2 model to determine the residual source power spectrum.

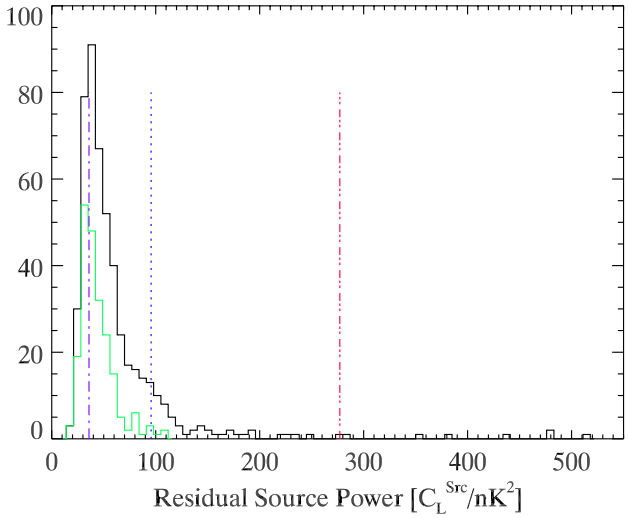

Figure 12. CBI residual source contamination, determined from low-frequency source counts plus GBT and OVRO 31 GHz information, via simulations described in the text. The heavy black line is the distribution full distribution and is our best prediction for random ∼140 deg^2 of sky. The light green distribution is for realizations which have no "orphan" sources which would have been detected in the CBI maps, and represents our best prediction for the residual source contribution to the CBI data. The residual source correction used in CBI analyses prior to this work is shown as a dotted blue line, the dash-dotted purple line is that calculated by Cleary et al. (2005) from VSA source counts at 31 GHz, and the red dash-double-dot line is the level of source contamination needed to fully account for the power that CBI observes in excess of intrinsic CMB anisotropy (Sievers et al. 2009). Note that the units of the x-axis are C_ℓ rather than $\ell(\ell+1)C_\ell/2\pi$.

(A color version of this figure is available in the online journal.)

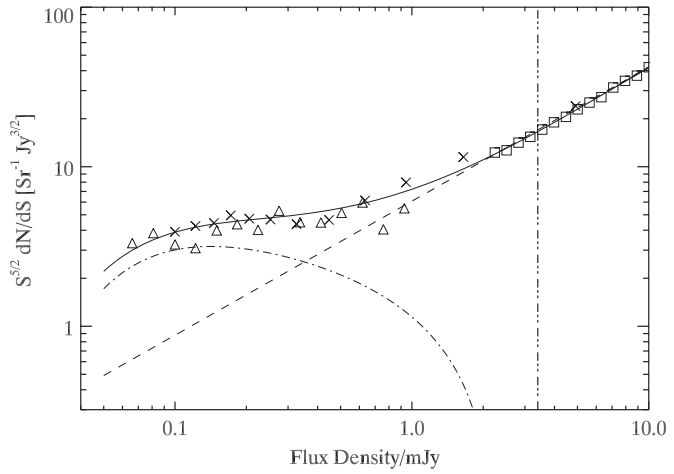

Figure 13. 1.4 GHz source counts. The solid line is the model of Hopkins et al. (2003) and triangles are their measurements in the Phoenix Deep Field; ×'s are the source counts from the COSMOS field (Bondi et al. 2008) and squares are source counts from FIRST (White et al. 1997). The dashed line is a power-law fit to the FIRST source counts at flux densities fainter than 100 mJy and the dot-dashed line is the excess of the full source counts over the power-law form. The vertical dash-double-dot line is the CBI projection threshold: the sources of interest are those to the left of this line. The power-law behavior persists up to 100 mJy.

The resulting estimate of the CBI residual source contamination is shown in Figure 12. We find the mean signal[7] from the clean simulations is $C_\ell^{\rm src} = 44 \pm 14$ nK^2; this is our best estimate of the residual point-source contamination in the CBI fields. In comparison, the mean signal from all simulations (neglecting the CBI/GBT orphan-source constraints) is 63^{+24}_{-30} nK^2. The 95% upper limits for the clean and total distributions are 80 nK^2 and 204 nK^2, respectively. The maximum power in any of the 215 clean simulations is 112 nK^2, or almost exactly half of what is needed to explain the excess power observed by CBI over intrinsic anisotropy, compared 519 nK^2 in the total set of simulation. For the total set of simulations, 2.2% of instances give power equal to or exceeding what is needed to account for the CBI high-ℓ excess. The long tail to high power in the total distribution comes from *one to a few individual bright 30 GHz sources* which would have been detected in the CBI maps were they present. The non-Gaussian nature of the distribution is substantial: the scatter in Gaussian simulations with the same average power as the clean simulations is a factor of 5.5 lower.

Our observed level is in good agreement with, though generally lower than, past measurements. Mason et al. (2003) found 0.08 ± 0.04 Jy^2 sr^{-1} ($C_\ell^{\rm src} = 96 \pm 48$ nK^2), the value used in previous CBI analyses, based on Owens Valley 40 m measurements. The data in Cleary et al. (2005) predict a mean level of 0.03 Jy^2 sr^{-1} ($C_\ell^{\rm src} = 36$ nK^2), with no uncertainty stated. These results are consistent with what we report here.

Sharp et al. (2009) recently reported a determination of residual source power $\ell(\ell+1)C_\ell^{\rm src}/(2\pi) = 378 \pm 87$ μK^2 following a procedure similar to ours with data from the Sunyaev–Zel'dovich Array (SZA). These results are also at 30 GHz but on smaller angular scales ($\ell \sim 4500$) where the discrete source power will be higher. Under the approximation that the flat-bandpower CMB window functions adequately represent the effect of sources on the power spectrum, we can compare these results to the results of our simulations above. Our best estimate of the residual (sub 3.4 mJy in NVSS) source contamination at 31 GHz for *random* fields on the sky is the total distribution neglecting the CBI map constraints, resulting in a predicted $\ell(\ell+1)C_\ell^{\rm src}/2\pi = 242^{+77}_{-97}$ μK^2 for the SZA measurement (including the extra contribution estimated in Section 5.3.2). Taking the SZA error bar at face value, these measurements are consistent at 1.2σ. The SZA error bar is based on Gaussian statistics so will be a significant underestimate of the true uncertainty in the residual source power spectrum. The underestimate is a factor of 5.5 for the CBI fields but will be different for the SZA since the size of the areas covered is very different. Conversely, were the entire CBI excess to be explained by discrete sources the SZA should see $\ell(\ell+1)C_\ell^{\rm src}/(2\pi) = 875 \pm 221$ μK^2. This is only marginally (2.1σ) consistent with the lower power level seen by the SZA.

5.3.2. The Contribution of Submillijansky Galaxies

Our simulations considered only the power-law-distributed source population which is seen at mJy levels and higher in low-frequency surveys. We must also consider the contribution of fainter sources likely belonging to a different population and having different spectral properties. At 1.4 GHz flux densities under ∼ 1 mJy, the source counts turn up due to the emergence of the high-z starbursting galaxies (e.g., Windhorst et al. 1985)—see Figure 13. We can estimate the impact of this population by first considering source correction at low frequency. Explicitly

[7] Previous CBI analyses expressed the residual source correction in the units implied by Equation (1), while here we express them in terms of C_ℓ, which is also independent of ℓ for unresolved sources but is more readily compared to other experiments. The conversion between $X_{\rm src}$ and $C_\ell^{\rm src}$ is given by $C_\ell^{\rm src} = X_{\rm src} \times \left[\frac{2k_B}{c^2}\left(\frac{k_B T_{\rm cmb}}{h}\right)^2 \frac{x^4 e^x}{(e^x-1)^2}\right]^{-2}$. Note that CMB bandpowers are typically expressed with the normalization $\ell(\ell+1)C_\ell/(2\pi)$. For reference, our result $C_\ell^{\rm src} = 43.0$ nK^2 corresponds to $X_{\rm src} = 0.036$ Jy^2 sr^{-1}, and at $\ell = 2500$, $\ell(\ell+1)C_\ell^{\rm src}/(2\pi) = 43.2$ μK^2.

integrating the source count of Hopkins et al. (2003) from 50 μJy to 3.4 mJy, we find a total 1.4 GHz residual source contribution of $C_\ell^{\rm src} = 1038$ nK^2. We assume that the turn-up is due to a distinct population. Integrating the power law over this range gives 869 nK^2, thus, the contribution of the sources responsible for the turn-up in the counts below a millijansky is 170 nK^2 at 1.4 GHz. This implies that if every single one of these sources had a flat spectrum between 1.4 and 31 GHz, they would account for less than two-thirds of the small-scale power in excess of the CMB observed by CBI of 270 nK^2. In reality, observations of μJy sources (Richards 2000) show typical spectral indices between 1.4 and 8 GHz of -0.8, consistent with the observed dominance of synchrotron in nearby starbursting galaxies (Yun & Carilli 2002; Condon 1992).

Assuming the distribution of spectral indices which we determined for mJy-level radio galaxies we obtain a 31 GHz value $C_\ell^{\rm src} = 12$ nK^2, a small correction to the mJy-AGN contribution of 44 nK^2. We include this contribution in the power spectrum analysis for a final correction of 56 nK^2. de Zotti et al. (2005) also find that submillijansky galaxies make a minor contribution in comparison to mJy-level AGN.

It is possible that the sources responsible for the turn-up in the low-frequency counts could have a high incidence of inverted-spectrum sources extending to 31 GHz thus contributing more to the high-ℓ source correction. Using simulations similar to those in Section 5.2 with modified spectral-index distributions we estimate that were these sources to have moderately inverted spectral ($\alpha \sim 0.2$) they would need to constitute 40% of the submillijansky population in order to fully explain the CBI excess. Were they to have strongly inverted spectra ($\alpha \sim 0.8$), 2% of the population is required. In contrast, most steeply inverted-spectrum sources in the GBT+OVRO surveys had $\alpha = 0.49$ and $< 0.1\%$ of sources had $\alpha > 0.3$. Both cases would give rise to substantial enhancements (factors of 1.5 and 3 for the strongly and moderately inverted cases, respectively) enhancements of the 31 GHz source counts over those reported in Section 5.2 in the 1–10 mJy range.

Preliminary analysis of deeper 31 GHz GBT (B. Mason et al. 2010, in preparation) and ATCA (A. Taylor et al. 2010, in preparation) observations targeting a small sample of ~ 40 sources with $S_{1.4} \sim 1$ mJy indicates that the mean 1.4–31 GHz spectral index of these sources is comparable to that of the AGN population and that there is not a substantial population with inverted spectra continuing to 31 GHz.

5.3.3. Source Clustering

In addition to the Poisson or shot noise contribution of discrete sources to the power spectrum, there will also be a contribution due to their spatial correlations, given by the second term of (Scott & White 1999; Oh et al. 2003)

$$C_\ell^{\rm src} \propto \int_0^{s_{\rm max}} ds\, s^2 \frac{dN}{ds} + \omega_\ell \left(\int_0^{s_{\rm max}} ds\, s \frac{dN}{ds} \right)^2 \quad (8)$$

$$\propto \langle s^2 \rangle + \langle s \rangle^2 \omega_\ell, \quad (9)$$

where ω_ℓ are the coefficients of the Legendre polynomial expansion of the discrete source angular correlation function (ACF) $\omega(\theta)$. The first term on the right-hand side of this equation is simply the shot noise contribution which has already been considered in detail. Using the Blake & Wall (2002) measurement of the NVSS ACF, and the value $\langle S_{31} \rangle^2 / \langle S_{31}^2 \rangle = 0.04$ determined from the 31 GHz flux density PDFs determined in Section 5.1, we find that clustering is a negligible contribution in comparison to the Poisson term at these faint flux densities. The submillijansky sources, which have a substantial contribution from starbursting galaxies, could be more strongly clustered than mJy AGN. Applying the 3σ upper limit of Webb et al. (2003) on the clustering amplitude of submillimeter galaxies to the sources lying above the AGN differential counts power law does not change the conclusion from the calculation.

5.3.4. Source Variability

Some sources exhibit significant time variability, with variability measures increasing to timescales of up to $\sim$2 years (Hughes et al. 1992). The effect of this will be to broaden our measurement of the apparent 1.4–31 GHz flux density ratio $r(t_1 - t_2) = S_{31}(t_2)/S_{1.4}(t_1)$ over what would be observed in a commensal multi-frequency survey, $r_0 = S_{31}(t_1)/S_{1.4}(t_1)$. Provided the 31 GHz measurements are separated from the 1.4 GHz measurements by a period of time greater than the longest characteristic timescale for variations, our measured distribution of r will be a statistically fair description of $S_{31}(t_3)/S_{1.4}(t_1)$ for other 31 GHz occurring at some time t_3 also separated from t_1 by greater than the longest characteristic timescale for variation. Considering that the 1.4 GHz NVSS observations were collected from 1993 September to 1996 October, the CBI observations from 1999 November to 2005 April, and the GBT observations from 2006 February to May, this will largely be the case. There could be a small number of variable sources with variability measures increasing beyond time spans of 10 years but compared to the sample as a whole these are rare and will have little impact on our results.

We note that while r is a fair sample to describe the CBI residual source power, extrapolations between frequencies other than 1.4 and 30 GHz will be biased. Even assuming that all sources instantaneously have true power-law spectra, sources whose apparent spectral indices fluctuate flatward due to variability make very different marginal contributions to the calculated sky variance at another frequency than those whose apparent spectral indices fluctuate steepward.

6. CONCLUSIONS

By measuring the 31 GHz flux densities of a large sample of 1.4 GHz selected sources, we have for the first time characterized the 31 GHz properties of a large sample of mJy-level radio galaxies. Our sample was large enough to place significant limits upon the frequency of rare inverted-spectrum sources which can contribute significantly to the 31 GHz counts, and even more to the 31 GHz sky variance. We find that the mean 31–1.4 GHz flux density ratio is 0.111 ± 0.003, corresponding to a spectral index -0.71 ± 0.01, and the mean spectral index is $< \alpha > = -0.92^{+0.29}_{-0.30}$. The fraction of sources with $\alpha > -0.5$ is $9.0\% \pm 0.8\%$ and the fraction with inverted spectral indices $\alpha > 0$ is $1.2\% \pm 0.2\%$. This has allowed us to greatly improve the accuracy with which we calculate the statical point-source correction for the CBI experiment. We find that residual mJy-level AGNs contribute a power of $C_\ell^{\rm src} = 44 \pm 14$ nK^2. Including an additional estimated 12 nK^2 contribution from faint "submillijansky" sources, residual sources account for $21\% \pm 7\%$ of the amplitude of the power seen in excess of intrinsic anisotropy by CBI at $\ell > 2000$. We place a 95% upper limit on residual source contamination of $C_\ell^{\rm src} = 92$ nK^2 or 34% of the total

excess power. By way of comparison, a total residual point-source correction 270 ± 60 nK^2 is needed to fully account for the observed CBI excess power. All of these results are consistent (at 1.2σ) with the recent SZA result of Sharp et al. (2009); a detailed comparison is given at the end of Section 5.3.1. Note that we express our results in terms of C_ℓ, which is appropriate for unresolved sources, rather than $\ell(\ell+1)C_\ell/2\pi$.

A population of faint inverted-spectrum sources not present at millijansky levels could compromise these conclusions, but the requirements are substantial: 20% of $S_{1.4} < 1$ mJy sources would need to have $\alpha_{1.4\text{–}30} = +0.2$, for instance, a factor of 20 more than is observed at mJy levels in this survey; or 2% of $S_{1.4} < 1$ mJy sources would need to have $\alpha_{1.4\text{–}30} = +0.8$, resulting in ∼8 of these sources per square degree above a millijansky at 30 GHz. In this survey of 3165 sources only a single source was as steeply inverted as $\alpha = 0.5$. Both scenarios would imply enhancements of the 31 GHz source counts over what we have measured by at least 50% at 1 mJy.

It is worth noting several points in connection with these conclusions. First, it is essential to appreciate that the residual sources are fundamentally selected by 1.4 GHz flux density. Second, for an unbiased calculation of the 31 GHz contribution of these sources a complete 1.4–31 GHz (effective) spectral-index distribution must be used. Populations *selected* at a higher frequency will have preferentially flatter spectral indices; and spectral indices measured between 1.4 and a higher frequency less than 31 GHz will not in general be representative, and in particular, will not reflect the steepening of synchrotron spectral indices to higher frequencies. Both of these effects, due to the large lever arm in frequency involved, have a significant impact. Third, it is essential to avoid selection biases in estimating the spectral-index distribution. In the absence of better information, previous CBI results used an incomplete sample of 1.4–31 GHz spectral indices (biased flat) resulting in an overestimate of the point-source contribution. The Bayesian analysis of Section 5.1 eliminates any bias due to censoring (non-detections) at 31 GHz. Fourth, as discussed in Section 5.3.4, spectral-index extrapolations from other frequencies are biased by source variability. Finally, it is important to use an accurate form of the well-known low-frequency counts rather than simple approximations to them. All of these considerations are independent of the 31 GHz counts per se, which are only indirectly related to the conclusions reached: to calculate the CBI residual source correction from 31 GHz counts requires the same additional information (the distribution of $S_{31}/S_{1.4}$) as calculating the statistical correction from the 1.4 GHz counts.

We have also computed 31 GHz counts based on 1.4 GHz source counts and our distribution of spectral indices, finding $N(>S_{31}) = 16.7 \pm 1.7 \times (S_{31}/10\ \mathrm{mJy})^{-0.80\pm0.07}$ deg^{-2} for 1 mJy $< S_{31} <$ 4 mJy, in good agreement with observed 31 GHz source counts at higher flux densities, as well as the model of de Zotti et al. (2005).

The National Radio Astronomy Observatory is a facility of the National Science Foundation operated under cooperative agreement by Associated Universities, Inc. We thank the GBT and OVRO science and engineering staff for outstanding contributions to both survey projects and acknowledge support from NSF grants AST-9413935, AST-9802989, AST-0098734, and AST0206416. We thank Gianfraco deZotti for providing us with his most recent 30 GHz source count model; Dan Marrone for providing the SZA window functions; Jim Condon, Bill Cotton, Mike Jones, and Angela Taylor for helpful discussions; and Rachel Rosen for carefully proofreading the manuscript. We thank Liz Waldram and Guy Pooley for providing unpublished source size information from the 9C survey. Finally, we thank an anonymous referee for thorough comments which helped to improve the paper.

APPENDIX A

CONFUSION CORRECTION

Consider that we have a set of $N_{\rm obs}$ potentially mutually confused measurements $S_{{\rm obs},i}$ and seek to determine the true flux densities $S_{T,i}$ of the targeted sources in the presence of a number of other contributing $N_{\rm est}$ sources for which we have no measurements, but only some uncertain flux density estimates $S_{{\rm est},j}$. These quantities are related by

$$\begin{pmatrix} S_{\rm obs,1} \\ S_{\rm obs,2} \\ \dots \\ S_{{\rm obs},Nobs} \end{pmatrix} = \begin{pmatrix} B_{11} & B_{12} & \dots & B_{1,Nobs} \\ B_{21} & B_{22} & \dots & B_{2,Nobs} \\ & \dots & & \\ B_{Nobs,1} & \dots & & B_{Nobs,Nobs} \end{pmatrix} \times \begin{pmatrix} S_{\rm True,1} \\ S_{\rm True,2} \\ \dots \\ S_{{\rm True},Nobs} \end{pmatrix} + \dots \quad \text{(A1)}$$

$$\begin{pmatrix} B_{11} & B_{12} & \dots & B_{1,Nest} \\ B_{21} & B_{22} & \dots & B_{2,Nest} \\ & \dots & & \\ B_{Nobs,1} & \dots & & B_{Nobs,Nest} \end{pmatrix} \begin{pmatrix} S_{\rm est,1} \\ S_{\rm est,2} \\ \dots \\ S_{{\rm est},Nest} \end{pmatrix},$$

where the B_{ij} is the beam weight that source j contributes to observation i, for a Gaussian beam

$$B_{ij} = \exp\left(-\frac{|\vec{x}_i - \vec{x}_j|^2}{2\sigma^2_{{\rm beam},i}}\right) \quad \text{(A2)}$$

for an observation pointed at $\vec{x}_i$ and a source at $\vec{x}_j$. $\sigma_{{\rm beam},i}$ is the Gaussian beamwidth for measurement i, potentially different for different measurements if the data come from different telescopes as is the case here. This is a straightforward system of $N_{\rm obs}$ equations in $N_{\rm obs}$ unknowns.

We must also account for our off-source (or reference) beam positions. Due to our position-nodded beam-switching observing strategy, and the fact that the beam switching occurs in azimuth, the reference (off-source) beams sweep out arcs on the sky giving a greater chance of encountering a second source; but tracking over a range of parallactic angles will cancel this effect on average. The OVRO data, with observations of a given source spread over many days or even months, sample a wide range of parallactic angles. Consequently, for the OVRO data we use the average reference beam arcs in calculating the B_{ij}. The GBT data, in contrast, typically have a single measurement at a well-defined parallactic angle for a given source.

Using the reference catalog, we scan the full set of OVRO observations and identify those for which the sum of the absolute values of beam-weighted confusing source flux densities in the reference catalog amounts to more than half the measurement error for that source. We solve Equation (A2) for this subset of observations and use the corrected values in the catalog; revised uncertainties are also calculated by propagating the measurement errors, assuming $\sigma(S_{\rm est}) = S_{\rm est}$ for the non-measured sources (determined from the distribution of $S_{31}/S_{1.4}$ of Section 5.1). For the OVRO data, this affects 1.3% of the data.

APPENDIX B

MAXIMUM LIKELIHOOD

We can rewrite the likelihood in terms of flux density ratios and use the fact that the measurement errors are uncorrelated to get

$$P\left(\frac{S_{31,\mathrm{obs}}}{S_{1.4,\mathrm{obs}}}\right) \propto \int dS_{31,T}\, P\left(S_{31,\mathrm{obs}}|S_{31,T}\right) \int P\left(\frac{S_{31,T}}{S_{1.4,T}}|S_{1.4,T}\right) \times P\left(\frac{S_{1.4,T}}{S_{1.4,\mathrm{obs}}}\right) dS_{1.4,T}. \quad \text{(B1)}$$

The outer integral is a convolution with the 31 GHz (OVRO and GBT) measurement error distribution; the inner integral folds the flux density ratio through the 1.4 GHz measurement error distribution, including a Malmquist-bias correction in the $P(S_{1.4,\mathrm{obs}}|S_{1.4,T})$ which assumes differential source counts of the form $S^{-1.66}$. Since the measurements of each source are independent, the total log-likelihood is the sum of the log-likelihoods for individual sources, and evaluating the likelihood reduces to (efficiently) evaluating the individual PDFs for all the 31 GHz flux density measurements (OVRO and GBT). We assume that $\frac{S_{31,T}}{S_{1.4,T}}$ is independent of the 1.4 GHz flux density over the range of interest, approximately 1–3.4 mJy.

Several points should be noted as follows.

1. Under the assumption (to be checked) that the $\frac{S_{31,T}}{S_{1.4,T}}$ distribution is independent of the 1.4 GHz flux density over the range of interest, we can take $P\left(\frac{S_{31,T}}{S_{1.4,T}}|S_{1.4,T}\right) \rightarrow P\left(\frac{S_{31,T}}{S_{1.4,T}}\right)$, i.e., the distribution is the same for all sources and needs to be calculated only once.
2. For computational efficiency, we precalculate the fast Fourier transform (FFT) of the inner integral, $P\left(\frac{S_{31,T}}{S_{1.4,\mathrm{obs}}}\right)$ for a range of 1.4 GHz signal-to-noise values at each likelihood step, then linearly interpolate between these values for a given source.
3. Calculating $P(S_{31,\mathrm{obs}}|S_{1.4,\mathrm{obs}})$ requires convolving $P(S_{31,\mathrm{true}})$ with the 31 GHz noise. We use the fact that we wish to evaluate $P(S_{31,\mathrm{observed}})$ only at the actual observed flux density to speed up the convolution. Because we calculate the Fourier transform of $P(S_{31,\mathrm{true}}|S_{1.4,\mathrm{observed}})$ in the previous step, the convolution with the (Gaussian) 31 GHz noise is an analytic multiplication. We evaluate the back transform only at the two FFT points bracketing the observed flux density, then linearly interpolate between them. This saves us from having to do a full FFT for each source, with computational load reduced from $N\log(N)$ to $2N$.
4. Because differences in log-likelihood are meaningful, the maximum-likelihood process naturally produces meaningful errors in the flux density distribution that fold in both the measurement errors and the uncertainty due to the finite number of sources measured.

We parameterize $\frac{S_{31,T}}{S_{1.4,T}}$ with a set of evenly spaced points in the frequency spectral index α, and do a piecewise-Hermite cubic polynomial interpolation through them, padded with zeros on either side. The Hermite interpolation is similar to a spline, but has two key advantages: the interpolation is always local so it never rings and the function values between interpolation points are always bracketed by the function values at points. So, as long as our model points stay non-negative, the interpolated PDF will also be strictly non-negative.

REFERENCES

Balser, D., Nikolic, B., & Prestage, R. 2006, GBT Technical Memo PTCS-PN/49.1
Blake, C., & Wall, J. 2002, MNRAS, 337, 993
Bondi, M., Ciliegi, P., Schinnerer, E., Smolcic, V., Jahnke, K., Carilli, C., & Zamorani, G. 2008, ApJ, 681, 1129
Cleary, K. A., et al. 2005, MNRAS, 360, 340
Condon, J. J. 1992, ARA&A, 30, 575
Condon, J. 2003, GBT Technical Memo PTCS-PN/26.3
Condon, J. J., Cotton, W. D., Greisen, E. W., Yin, Q. F., Perley, R. A., Taylor, G. B., & Broderick, J. J. 1998, AJ, 115, 1693
de Zotti, G., Ricci, R., Mesa, D., Silva, L., Mazzotta, P., Toffolatti, L., & González-Nuevo, J. 2005, A&A, 431, 893
Dennett-Thorpe, J., Bridle, A. H., Laing, R. A., & Scheuer, P. A. G. 1999, MNRAS, 304, 271
Hill, R. S., et al. 2009, ApJS, 180, 246
Hoaglin, D., Mosteller, F., & Tukey, J. 1983, Understanding Robust and Exploratory Data Analysis (New York: Wiley)
Hopkins, A. M., Afonso, J., Chan, B., Cram, L. E., Georgakakis, A., & Mobasher, B. 2003, AJ, 125, 465
Hughes, P. A., Aller, H. D., & Aller, M. F. 1992, ApJ, 396, 469
Jarosik, N., et al. 2003, ApJS, 145, 413
Jewell, P. R., & Prestage, R. M. 2004, Proc. SPIE, 5489, 312
Kovac, J. M., Leitch, E. M., Pryke, C., Carlstrom, J. E., Halverson, N. W., & Holzapfel, W. L. 2002, Nature, 420, 772
Laing, R. A., & Peacock, J. A. 1980, MNRAS, 190, 903
Leitch, E. M., Readhead, A. C. S., Pearson, T. J., Myers, S. T., & Gulkis, S. 2000, ApJ, 532, 37
Lewis, A., & Bridle, S. 2002, Phys. Rev. D, 66, 103511
Mason, B. S., et al. 2003, ApJ, 591, 540
Myers, S. T., et al. 2003, ApJ, 591, 575
Oh, S. P., Cooray, A., & Kamionkowski, M. 2003, MNRAS, 342, L20
Padin, S. 2001, Caltech Technical Memo
Pearson, T. J., et al. 2003, ApJ, 591, 556
Readhead, A. C. S., Lawrence, C. R., Myers, S. T., Sargent, W. L. W., Hardebeck, H. E., & Moffet, A. T. 1989, ApJ, 346, 566
Readhead, A. C. S., et al. 2004, ApJ, 609, 498
Richards, E. A. 2000, ApJ, 533, 611
Scott, D., & White, M. 1999, A&A, 346, 1
Sharp, M. K., et al. 2009, arXiv:0901.4342
Sievers, J. L., et al. 2007, ApJ, 660, 976
Sievers, J., et al. 2009, ApJ, submitted (arXiv:0901.4540)
Toffolatti, L., Argueso Gomez, F., de Zotti, G., Mazzei, P., Franceschini, A., Danese, L., & Burigana, C. 1998, MNRAS, 297, 117
Webb, T. M., et al. 2003, ApJ, 587, 41
White, R. L., Becker, R. H., Helfand, D. J., & Gregg, M. D. 1997, ApJ, 475, 479
Windhorst, R. A., Miley, G. K., Owen, F. N., Kron, R. G., & Koo, D. C. 1985, ApJ, 289, 494
Yun, M. S., & Carilli, C. L. 2002, ApJ, 568, 88